nature materials

LETTERS

PUBLISHED ONLINE: 19 AUGUST 2012 | DOI: 10.1038/NMAT3405

Quantum many-body interactions in digital oxide superlattices

Eric J. Monkman[1†], Carolina Adamo[2†], Julia A. Mundy[3], Daniel E. Shai[1], John W. Harter[1], Dawei Shen[1], Bulat Burganov[1], David A. Muller[3,4], Darrell G. Schlom[2,4] and Kyle M. Shen[1,4*]

Controlling the electronic properties of interfaces has enormous scientific and technological implications and has been recently extended from semiconductors to complex oxides that host emergent ground states not present in the parent materials[1–5]. These oxide interfaces present a fundamentally new opportunity where, instead of conventional bandgap engineering, the electronic and magnetic properties can be optimized by engineering quantum many-body interactions[5–7]. We use an integrated oxide molecular-beam epitaxy and angle-resolved photoemission spectroscopy system to synthesize and investigate the electronic structure of superlattices of the Mott insulator $LaMnO_3$ and the band insulator $SrMnO_3$. By digitally varying the separation between interfaces in $(LaMnO_3)_{2n}/(SrMnO_3)_n$ superlattices with atomic-layer precision, we demonstrate that quantum many-body interactions are enhanced, driving the electronic states from a ferromagnetic polaronic metal to a pseudogapped insulating ground state. This work demonstrates how many-body interactions can be engineered at correlated oxide interfaces, an important prerequisite to exploiting such effects in novel electronics.

Exotic magnetic phases[1], high-T_c superconductivity[2], and two-dimensional correlated electron systems[3–5] are only a few examples of novel states recently realized at complex oxide interfaces. Although the electronic properties of conventional semiconductor heterostructures can be described by one-electron theories, performing such calculations for correlated materials is far more challenging because of competing many-body interactions. Understanding these correlated interfaces has been complicated by the inability to probe their underlying electronic structure and quantum many-body interactions[6,7], necessitating the development of new advanced spectroscopic probes.

Here we employ a combination of oxide molecular-beam epitaxy (MBE) and angle-resolved photoemission spectroscopy (ARPES) using an integrated system to first engineer and then investigate digital superlattices of $(LaMnO_3)_{2n}/(SrMnO_3)_n$. Owing to the surface sensitivity of ARPES, it has not yet been possible to measure atomically pristine oxide interfaces. Our integrated system circumvents this problem by allowing synthesis and measurement within the same ultrahigh vacuum manifold, avoiding any surface contamination. The manganites present an ideal case for modifying electronic and magnetic properties through interfacial engineering owing to their competing interactions and wide variety of ground states[8]. Bulk $LaMnO_3$ and $SrMnO_3$ are antiferromagnetic Mott and band insulators, respectively, and $La_{2/3}Sr_{1/3}MnO_3$ is a ferromagnetic metal that exhibits colossal magnetoresistance around its Curie temperature of 370 K. Increasing the separation between the $LaMnO_3$ and $SrMnO_3$ layers with integer n has been shown to drive a crossover from a ferromagnetic metallic ($n < 3$) to a ferromagnetic insulating ground state ($n \geq 3$; refs 9–11) whose origin is currently not understood, as theoretical studies predict metallic interfaces for large n (refs 12,13).

The tunability of oxide heterostructures can arise either from controlling band alignments or structural potentials, as is achieved in conventional semiconductors, or by taking advantage of the strong many-body interactions that are uniquely accessible in correlated materials. We use ARPES to reveal that although the band structure remains largely unchanged with interfacial separation, a large pseudogap is opened within 800 meV of E_F for $n = 3$, and closes either on warming into the paramagnetic state or reducing the interfacial separation ($n \leq 2$). Our work provides the first direct observation of how quantum many-body interactions can be engineered in artificial materials constructed with atomic-layer precision to control the electronic ground state.

In Fig. 1, we show **k**-resolved spectral weight maps for the $n = 1$, 2 and 3 samples of $(LaMnO_3)_{2n}/(SrMnO_3)_n$. All films were terminated with n layers of $SrMnO_3$ with a MnO_2 surface (Fig. 1d), and are expected to be non-polar owing to their inversion symmetric structure. In Fig. 1a,b, the Fermi surfaces of the metallic $n = 1$ and 2 materials are apparent and consist of two Mn e_g derived states: a hole pocket of predominantly $d_{x^2-y^2}$ character around the Brillouin zone corner, and a smaller electron pocket of primarily $d_{3z^2-r^2}$ character around the zone centre. For the insulating $n = 3$ sample, the spectral weight at E_F is suppressed, although clear states are still observed below E_F. In Fig. 1d–f we show elementally resolved scanning transmission electron micrographs of the same samples measured by ARPES, demonstrating atomically abrupt $LaO/MnO_2/SrO$ and $SrO/MnO_2/LaO$ interfaces. In Fig. 1g, we show the resistivity for $n = 1$, 2 and 3 superlattices grown using the same approach[11], showing the metal–insulator crossover for $n \geq 3$. In Fig. 1h, the valence bands of $n = 1$, 2 and 3 are shown.

We observe that the electron pocket decreases in size as n increases in Fig. 1a–c, indicating the preferential filling of $d_{x^2-y^2}$ orbitals, suggesting an approach towards an interfacial two-dimensional electronic structure. To quantify these changes, we fit the measured Fermi surfaces and dispersions to a simple tight-binding parametrization (Supplementary Information), shown in Fig. 2 and overlaid onto data in Figs 3 and 4. Estimating the carrier density from counting the Luttinger volume of the Fermi surfaces gives higher hole concentrations ($x \approx 0.5 \pm 0.1$) than would be expected from a random alloy ($x = 0.33$), as

[1]Laboratory of Atomic and Solid State Physics, Department of Physics, Cornell University, Ithaca, New York 14853, USA, [2]Department of Materials Science and Engineering, Cornell University, Ithaca, New York 14853, USA, [3]School of Applied and Engineering Physics, Cornell University, Ithaca, New York 14853, USA, [4]Kavli Institute at Cornell for Nanoscale Science, Ithaca, New York 14853, USA. †These authors contributed equally to this work.
*e-mail: kmshen@cornell.edu.

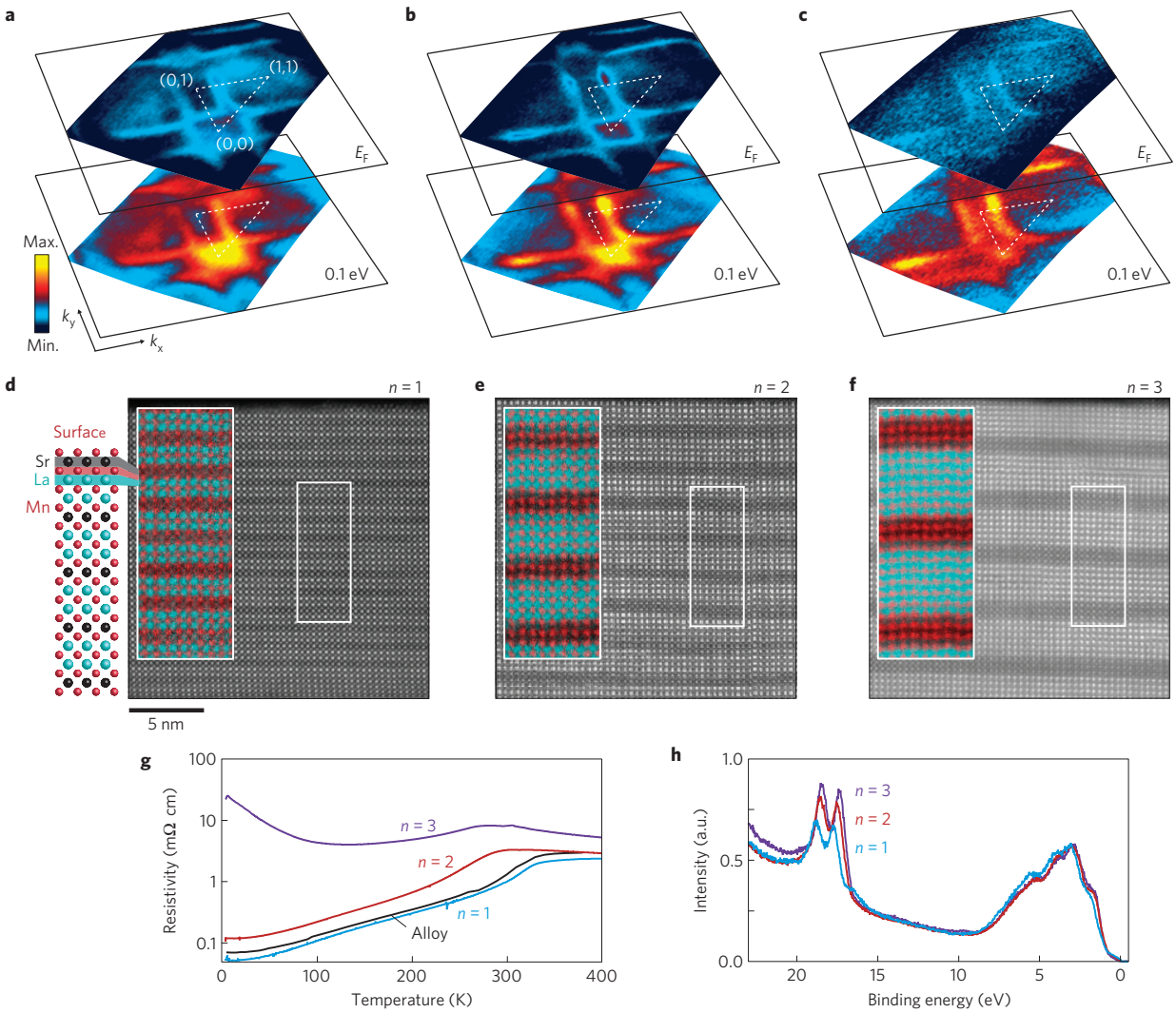

Figure 1 | Overview of the superlattices' electronic structure and properties. a–c, **k**-resolved maps of photoemission spectral weight for $(LaMnO_3)_{2n}/(SrMnO_3)_n$ with $n = 1$, 2 and 3 respectively, at $T = 10$ K. Maps are at E_F and 0.1 eV binding energy as indicated. **d–f**, High-angle annular dark-field scanning transmission electron micrographs of $n = 1$, 2 and 3 samples that were measured by ARPES, along with a schematic of the $n = 1$ structure with MnO_2 surface termination. Enlarged electron energy-loss spectroscopic images (insets) show La in turquoise and Mn in red, and demonstrate well-ordered films with clear separation of Sr and La. Distortions in the electron energy-loss map are not structural, but are artefacts from sample drift during data acquisition. Images over a very wide field of view can be found in the Supplementary Information. **g**, Resistivity of superlattices as a function of n and temperature showing the crossover to insulating behaviour at $n = 3$ (data from ref. 11). Also shown for comparison, the resistivity of a random alloy $La_{2/3}Sr_{1/3}MnO_3$ film grown under identical conditions. **h**, The valence bands of the three superlattices are nearly identical over a wide energy range, except for the increasing intensity of the Sr 4*p* core states around 18 eV due to the termination of each superlattice by n unit cells of $SrMnO_3$.

expected from a $LaMnO_3/SrMnO_3$ interface. From our tight-binding wavefunctions, we can also estimate the orbital polarization defined as $(N_{(x^2-y^2)} - N_{(3z^2-r^2)})/(N_{(x^2-y^2)} + N_{(3z^2-r^2)})$, where N is the integral of the partial density of states up to E_F. The orbital polarization increases from 0% for cubic $La_{2/3}Sr_{1/3}MnO_3$ to approximately 50% for $n = 3$, consistent with X-ray absorption measurements that find $d_{x^2-y^2}$ polarization at the interfaces[14]. This polarization is dominated by the $d_{x^2-y^2}$ character of the hole-like sheets, although our orbital polarization never approaches 100% because their tight-binding wavefunctions still retain non-negligible $d_{3z^2-r^2}$ character. Despite its simplicity, our tight-binding model should qualitatively describe the change in orbital polarization with n, although more sophisticated density functional calculations would be necessary to obtain more accurate wavefunctions.

In Figs 3 and 4, we show the quasiparticle dispersion in energy versus momentum along cuts shown in the insets of Figs 3a and 4a. The $n = 1$ and 2 samples exhibit well-defined and dispersive bands (Fig. 3a,b). A sharp quasiparticle peak can only be observed for $n = 2$ (Fig. 4) and, owing to photoelectron final state effects[15], can be attributed to the interfacial states increasing confinement to two dimensions with n. The peak–dip–hump structure, where the coherent quasiparticle peak is dominated by a broad hump of incoherent spectral weight, is a signature of correlated systems and has been observed in the cuprates[16] and other manganites[17]. Figure 3e shows a kink in the dispersion for the $n = 2$ $d_{x^2-y^2}$ band within 35 meV of E_F. The ratio of band velocities at high and low energy gives $v_{F,high}/v_{F,low} = 3.7 \pm 0.6$. Within a weak-coupling scenario, this would correspond to a mass renormalization $m^*/m_{band} = 3.7$, although this falls well into the strong coupling regime. Similar features have been observed in other correlated systems that exhibit strong electron–boson interactions, such as the cuprates[16], and some bilayer manganites, where a similar velocity renormalization was observed at nearly the same energy ($v_{F,high}/v_{F,low} = 5.6$) and was attributed to strong electron–phonon coupling[17].

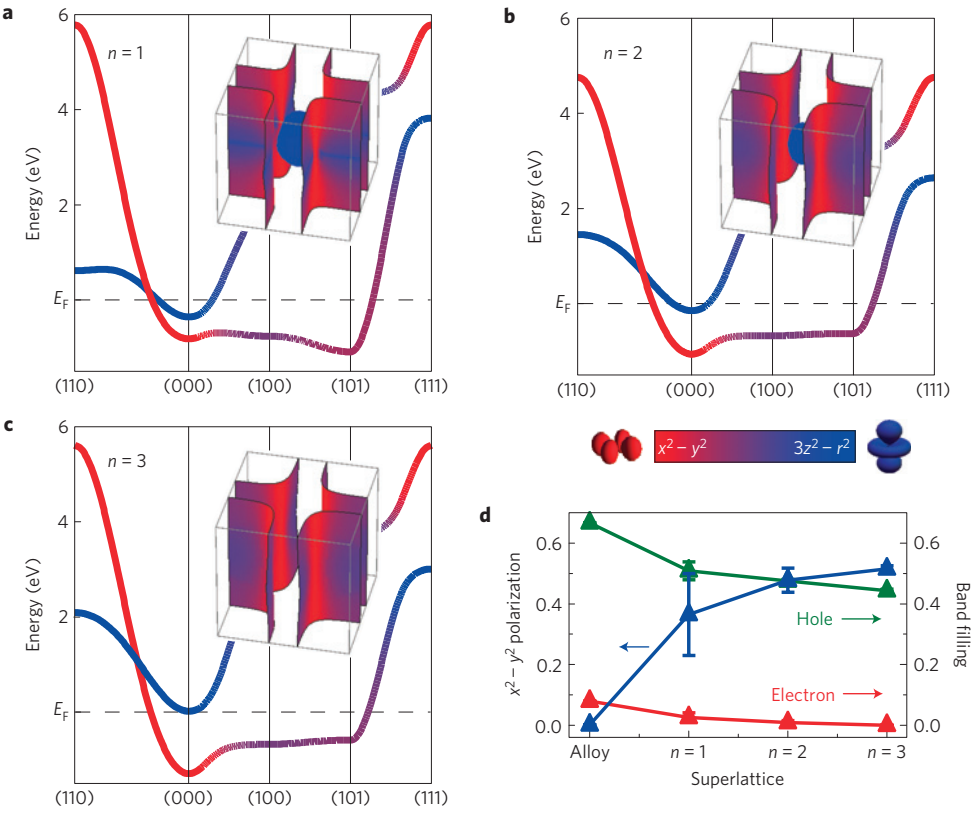

Figure 2 | The tight-binding parametrization. a–c, Tight-binding bandstructures and Fermi surfaces extracted from our ARPES data for the $n = 1$, 2 and 3 superlattices. The orbital character throughout the Brillouin zone is indicated by each band's colour. **d**, Orbital polarization and filling of the electron and hole pockets from the tight-binding model for the three superlattices and the random alloy. Error bars are determined from the maximum and minimum estimated size of the electron pocket from our ARPES data, which dominates the uncertainty of the tight-binding model (Supplementary Information).

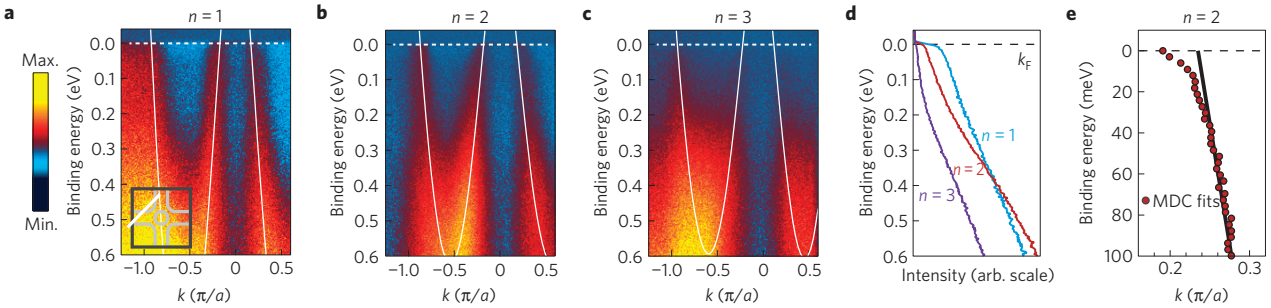

Figure 3 | Electronic structure of the hole pockets. a–c, ARPES spectra along the **k**-path illustrated by the inset of **a** (in units of π/a with $a = 3.905$ Å), showing the hole-pocket band crossing E_F at three points. Tight-binding fits are overlaid in white as guides to the eye. A non-dispersive background has been subtracted from the ARPES data to more clearly illustrate the bandstructure (Supplementary Information). **d**, Energy distribution curves (EDCs) of photoemission intensity at $\mathbf{k}_F$ of the hole pocket. **e**, ARPES band dispersion for $n = 2$ compared to the linear extrapolation of the dispersion for $E > 0.075$ eV, showing a kink at 35 meV.

Unlike the metallic superlattices, $n = 3$ exhibits only pseudogapped intensity at E_F (Fig. 3d), similar to polaronic systems with strong electron–phonon coupling[18,19]. Although the total spectral weight is generally conserved, the weight at low-energies is pushed to higher energy scales, which may then be obscured by the valence band. Despite the pseudogap, the $n = 3$ sample still exhibits the underlying hole-like $d_{x^2-y^2}$ dispersion at higher binding energies, with a comparable bandwidth and similar remnant Fermi surface to the $n = 1$ and 2 samples, as shown in Fig. 1c.

The similar dispersion of $n = 3$ to $n = 1$ and 2 demonstrates that the insulating behaviour is not caused by the opening of a conventional bandgap, as might be the case in semiconductor interfaces, and is consistent with resonant scattering measurements[20]. This suggests the pseudogap is the origin of the n-driven metal–insulator crossover, also supported by our temperature-dependent measurements (Fig. 5c). The metallic $n = 2$ superlattice shows a reduction in weight near E_F with increasing temperature, consistent with a loss of coherent quasiparticles in the paramagnetic state. On the other hand, the spectral weight of $n = 3$ increases above T_c as the pseudogap fills in, consistent with its resistivity approaching that of the metallic superlattices in the paramagnetic state.

A variety of reasons indicate our ARPES measurements of the topmost interfaces are representative of the bulk properties. First, we observe states at E_F for the metallic $n = 1$ and 2 superlattices, whereas the insulating $n = 3$ superlattice exhibits a pseudogap. Second, we observe a correspondence between the temperature

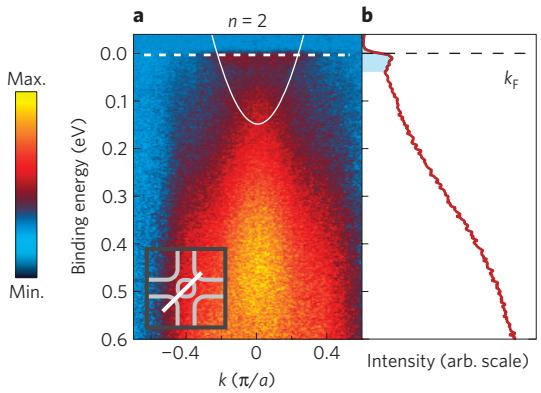

Figure 4 | Strongly renormalized quasiparticle peak. a, ARPES spectra along the **k**-path illustrated by the inset of **a** for the $n = 2$ superlattice. The tight-binding band for the electron pocket is shown by the white line as a guide to the eye. A non-dispersive background has been subtracted from the ARPES data to more clearly illustrate the bandstructure (Supplementary Information). **b**, EDC at $\mathbf{k}_F$ of the electron pocket. The quasiparticle peak is schematically illustrated by the blue shaded area.

dependence of our spectra and the bulk Curie temperature. Third, measurements of $SrMnO_3$ and $LaMnO_3$ films (Supplementary Information) do not exhibit any of the near-E_F electronic structure of the superlattices, which thus must arise from the $LaMnO_3/SrMnO_3$ interface. Fourth, Fermi surface volumes give hole concentrations close to $x = 0.50$, as might be expected from the $LaMnO_3/SrMnO_3$ interface, as opposed to $x = 0.33$. Fifth, the near-E_F suppression of spectral weight for $n = 3$ versus $n = 1$ is highly dependent on energy close to E_F (Fig. 5a,b), suggesting that this effect should not be due to surface sensitivity, as λ_{mfp} is effectively energy-independent in such a narrow range. Finally, our low-energy electron diffraction (LEED) and reflection high-energy electron diffraction (RHEED) patterns show 2×4 and 3×3 reconstructions associated with the $SrMnO_3$ termination (Supplementary Information), but the ARPES data do not exhibit any evidence of such a periodicity, again suggesting that the near-E_F states arise from the buried interface.

It has been suggested that reduced dimensionality could drive the $n \geq 3$ superlattices to become insulating via Anderson localization[12], where a Coulomb gap could form because of interactions between localized electrons. Despite their suppressed intensity, we observe well-defined bands for $n = 3$, demonstrating states that are delocalized over more than 8×8 unit cells ($\Delta k < 1/8$ of the Brillouin zone), outside of the conventional scenario for the Coulomb gap[21] or Anderson localization[22]. Our density of states near E_F (which follows $\approx \omega^2$) also deviates from the linear dependence expected for a two-dimensional Coulomb gap, whereas transmission electron microscopy measurements demonstrate a nearly disorder-free structure. Furthermore, a change in the hole concentration would not explain the crossover at higher n, as $La_{1-x}Sr_xMnO_3$ has no ferromagnetic insulating state at large x.

It is then natural to consider the quantum many-body interactions that are inherent to the manganites as the origin of the metal–insulator crossover observed with n. These interactions are known to give rise to insulating ordered states, as the effective dimensionality (that is, coupling along the c axis) is lowered in the Ruddlesden–Popper series of manganites, $(La, Sr)_{m+1}Mn_mO_{3m+1}$, where m is the number of MnO_2 planes per unit cell[23]. Bilayer $La_{2-2x}Sr_{1+2x}Mn_2O_7$ ($m = 2$) is a pseudogapped ferromagnetic 'bad metal' with a low-temperature resistivity two orders of magnitude higher than the metallic 3D perovskite ($m = \infty$). The quasi-two-dimensional $m = 1$ compound $La_{1-x}Sr_{1+x}MnO_4$ is insulating for all Sr concentrations[8,23] owing to the formation of charge, spin or orbital order[23,24], and exhibits a fully gapped spectral weight at E_F and a remnant Fermi surface observed by ARPES in $La_{0.5}Sr_{1.5}MnO_4$ (ref. 25).

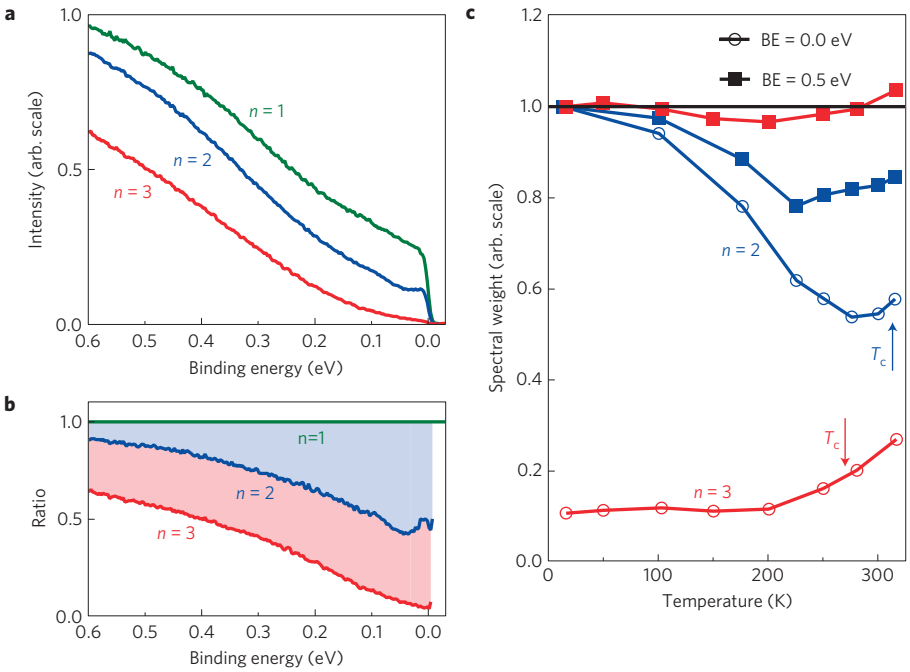

Figure 5 | The pseudogap and temperature-dependent spectral weight. a, The angle-integrated spectral weight for the $n = 1$, 2 and 3 superlattices, showing pseudogap behaviour in the $n = 3$ film. **b**, The data from **a** normalized to the spectral weight of the $n = 1$ superlattice, highlighting the strong energy dependence of the pseudogap. **c**, Temperature dependence of the spectral weight at the Brillouin zone centre for the $n = 2$ and 3 superlattices. Open circles show the spectral weight within 50 meV of E_F, filled squares show the spectral weight at a binding energy (BE) of 400–550 meV. Also indicated in **c** are the Curie temperatures (T_c) of each material. Data in **c** are normalized to unity at 20 K, except for the $n = 3$ open circles. Here, $n = 3$ data are normalized such that the integrated weight over E_F to 8.4 eV is equal to the $n = 2$ integral over the same window to allow a meaningful comparison between the two films.

Our measurements demonstrate that dimensionality also plays a similar role in the superlattices, as the partially occupied interfacial states become progressively separated and two-dimensional with increasing n as the effective hopping between interfaces is reduced. The similarities between their spectral features indicate the many-body interactions responsible for the properties of the single-layer and bilayer manganites are also paramount for the superlattices. The small quasiparticle weight and kink observed in the $n = 2$ superlattice suggests a metallic state consisting of coherent polarons that are strongly coupled to the lattice, orbital and/or magnetic degrees of freedom that reduce the quasiparticle residue[16–18]. Recent calculations also suggest that electron–lattice coupling should strongly influence the properties of manganite superlattices and interfaces[26,27]. Reducing the dimensionality from $n = 2$ to 3 results in a situation where the lowered dimensionality and possibly increased nesting in two dimensions may enhance quantum fluctuations towards the insulating charge, spin and orbitally ordered states, such as those observed in the single-layer $m = 1$ manganites[18,28]. These quantum fluctuations can disrupt the coherence of the fragile polaronic metallic state, giving rise to the weakly insulating/bad metal state observed in the bilayer manganites, as proposed in refs 19,29, thereby resulting in the pseudogap and loss of coherent quasiparticle weight in the $n = 3$ superlattice.

Our measurements of $(LaMnO_3)_{2n}/(SrMnO_3)_n$ superlattices demonstrate how the interplay of interactions and dimensionality can be used to control the properties of correlated oxide interfaces. By decoupling the $LaMnO_3/SrMnO_3$ interfaces, we are able to reduce the effective dimensionality, driving the polaronic metal at small n into a pseudogapped insulator. Demonstrating both the control and understanding of the interactions at these correlated interfaces should be a key step towards the rational manipulation and optimization of their functionality for potential applications.

Methods

$(LaMnO_3)_{2n}/(SrMnO_3)_n$ films of 20–25 nm thickness were grown on (100) $SrTiO_3$ substrates by MBE in two different systems: a dual chamber Veeco 930 MBE and a dual chamber Veeco GEN10 MBE, both equipped with reflection high-energy electron diffraction. Immediately after growth, they were transferred through ultrahigh vacuum to our ARPES chamber in under 300 s. All films were terminated with n layers of $SrMnO_3$. Further details on growth and characterization can be found in the Supplementary Information.

ARPES measurements were performed with a VG Scienta R4000 electron analyser and a VUV5000 helium plasma discharge lamp and monochromator, using 40.8 eV photons. The base pressure of the ARPES system was 4×10^{-11} torr, and data were taken at below 20 K unless specified otherwise. Constant-energy maps (Fig. 1) consist of 2×10^4 spectra integrated within ± 30 meV of the specified energy and taken with an energy resolution of 40 meV. Measurements of the quasiparticle dispersion, as presented in Figs 3 and 4, were taken with a resolution of 10 meV.

Electron energy-loss spectroscopic imaging and high-angle annular dark-field scanning transmission electron microscopy images were recorded from cross-sectional specimens in the 100 keV NION UltraSTEM. The Mn concentration is the integrated Mn–$L_{2,3}$ edge, the La concentration is the integrated $M_{4,5}$.

Received 13 March 2012; accepted 19 July 2012; published online 19 August 2012

References

1. Chakhalian, J. *et al.* Magnetism at the interface between ferromagnetic and superconducting oxides. *Nature Phys.* **2,** 244–248 (2006).
2. Logvenov, G., Gozar, A. & Bozovic, I. High-temperature superconductivity in a single copper–oxygen plane. *Science* **326,** 699–702 (2009).
3. Ohtomo, A. & Hwang, H. Y. A high-mobility electron gas at the $LaAlO_3/SrTiO_3$ heterointerface. *Nature* **427,** 423–426 (2004).
4. Okamoto, S. & Millis, A. J. Electronic reconstruction at an interface between a Mott insulator and a band insulator. *Nature* **428,** 630–633 (2004).
5. Jang, H. W. *et al.* Metallic and insulating oxide interfaces controlled by electronic correlations. *Science* **331,** 886–889 (2011).
6. Chakhalian, J., Millis, A. J. & Rondinelli, J. Whither the oxide interface. *Nature Mater.* **11,** 92–94 (2011).
7. Dagotto, E. When oxides meet face to face. *Science* **318,** 1076–1077 (2007).
8. Dagotto, E., Hotta, T. & Moreo, A. Colossal magnetoresistant materials: The key role of phase separation. *Phys. Rep.* **344,** 1–153 (2001).
9. Salvador, P. A., Haghiri-Gosnet, A-M., Mercey, B., Hervieu, M. & Raveau, B. Growth and magnetoresistive properties of $(LaMnO_3)_m(SrMnO_3)_n$ superlattices. *Appl. Phys. Lett.* **75,** 2638–2640 (1999).
10. Bhattacharya, A. *et al.* Metal–insulator transition and its relation to magnetic structure in $(LaMnO_3)_{2n}/(SrMnO_3)_n$ superlattices. *Phys. Rev. Lett.* **100,** 257203 (2008).
11. Adamo, C. *et al.* Tuning the metal–insulator transitions of $(SrMnO_3)_n/(LaMnO_3)_{2n}$ superlattices: Role of interfaces. *Phys. Rev. B* **79,** 045125 (2009).
12. Dong, S. *et al.* Magnetism, conductivity, and orbital order in $(LaMnO_3)_{2n}/(SrMnO_3)_n$ superlattices. *Phys. Rev. B* **78,** 201102 (2008).
13. Nanda, B. R. K. & Satpathy, S. Electronic and magnetic structure of the $(LaMnO_3)_{2n}/(SrMnO_3)_n$ superlattices. *Phys. Rev. B* **79,** 054428 (2009).
14. Aruta, C. *et al.* Evolution of magnetic phases and orbital occupation in $(SrMnO_3)_n/(LaMnO_3)_{2n}$ superlattices. *Phys. Rev. B* **80,** 140405 (2009).
15. Krempasky, J. *et al.* Effects of three-dimensional band structure in angle- and spin-resolved photoemission from half-metallic $La_{2/3}Sr_{1/3}MnO_3$. *Phys. Rev. B* **77,** 165120 (2008).
16. Damascelli, A., Hussain, Z. & Shen, Z-X. Angle-resolved photoemission studies of the cuprate superconductors. *Rev. Mod. Phys.* **75,** 473–541 (2003).
17. Mannella, N. *et al.* Nodal quasiparticle in pseudogapped colossal magnetoresistive manganites. *Nature* **438,** 474–478 (2005).
18. Chuang, Y-D., Gromko, A. D., Dessau, D. S., Kimura, T. & Tokura, Y. Fermi surface nesting and nanoscale fluctuating charge/orbital ordering in colossal magnetoresistive oxides. *Science* **292,** 1509–1513 (2001).
19. Massee, F. *et al.* Bilayer manganites reveal polarons in the midst of a metallic breakdown. *Nature Phys.* **7,** 978–982 (2011).
20. Smadici, S. *et al.* Electronic reconstruction at $SrMnO_3$–$LaMnO_3$ superlattice interfaces. *Phys. Rev. Lett.* **99,** 196404 (2007).
21. Efros, A. L. & Shklovskii, B. I. Coulomb gap and low temperature conductivity of disordered systems. *J. Phys. C* **8,** L49–L51 (1975).
22. Edwards, P. P. & Sienko, M. J. Universality aspects of the metal–nonmetal transition in condensed media. *Phys. Rev. B* **17,** 2575–2581 (1978).
23. Moritomo, Y. *et al.* Giant magnetoresistance of manganese oxides with a layered perovskite structure. *Nature* **380,** 141–144 (1996).
24. Larochelle, S. *et al.* Structural and magnetic properties of the single-layer manganese oxide $La_{1-x}Sr_{1+x}MnO_4$. *Phys. Rev. B* **71,** 024435 (2005).
25. Evtushinsky, D. V. *et al.* Bridging charge-orbital ordering and Fermi surface instabilities in half-doped single-layered manganite $La_{0.5}Sr_{1.5}MnO_4$. *Phys. Rev. Lett.* **105,** 147201 (2010).
26. Lin, C. & Millis, A. J. Theory of manganite superlattices. *Phys. Rev. B* **78,** 184405 (2008).
27. Iorio, A., Perroni, C. A., Marigliano Ramaglia, V. & Cataudella, V. Electron-lattice and strain effects in manganite heterostructures: The case of a single interface. *Phys. Rev. B* **83,** 085107 (2011).
28. Trinckauf, J. *et al.* Electronic confinement and ordering instabilities in colossal magnetoresistive bilayer manganites. *Phys. Rev. Lett.* **108,** 016403 (2012).
29. Salafranca, J., Gonzalo, A. & Dagotto, E. Electron-lattice coupling and partial nesting as the origin of Fermi arcs in manganites. *Phys. Rev. B* **80,** 155133 (2009).

Acknowledgements

We thank L. Fitting Kourkoutis for helpful discussions and E. Kirkland for technical assistance. This work was supported by the National Science Foundation (DMR-0847385), the Materials Research Science and Engineering Centers program through DMR-1120296, IMR-0417392 and DMR-9977547 (Cornell Center for Materials Research), a Research Corporation Cottrell Scholars award (20025), and New York State Office of Science, Technology and Academic Innovation (NYSTAR). J.A.M. acknowledges support from the Army Research Office in the form of a NDSEG fellowship. E.J.M. acknowledges the Natural Sciences and Engineering Research Council of Canada for PGS support.

Author contributions

ARPES data was collected by E.J.M., D.E.S., J.W.H., D.S., B.B. and K.M.S. and analysed by E.J.M. and K.M.S. Film growth and X-ray diffraction were performed by C.A. Electron microscopy and spectroscopy measurements were performed by J.A.M. and D.A.M. The manuscript was prepared by E.J.M. and K.M.S. The study was planned and supervised by D.G.S. and K.M.S. All authors discussed results and commented on the manuscript.

Additional information

Supplementary information is available in the online version of the paper. Reprints and permissions information is available online at www.nature.com/reprints. Correspondence and requests for materials should be addressed to K.M.S.

Competing financial interests

The authors declare no competing financial interests.